

1                   **Waveform detection by deep learning reveals multi-area spindles that are**  
2                   **selectively modulated by memory load**

4                   **Authors:** Maryam H. Mofrad<sup>1,2</sup>, Greydon Gilmore<sup>2,3</sup>, Seyed M. Mirsattari<sup>4,5,6,7</sup>, Jorge G. Burneo<sup>4,8</sup>,  
5                   David A. Steven<sup>4,8</sup>, Ali Khan<sup>2,3,6</sup>, Ana Suller Marti<sup>2,4</sup>, Lyle Muller<sup>1,2,†</sup>

6  
7                   **Affiliations:** <sup>1</sup>Department of Applied Mathematics, Western University, London, ON, Canada,  
8                   <sup>2</sup>Brain and Mind Institute, Western University, London, ON, Canada, <sup>3</sup>Department of Biomedical  
9                   Engineering, Western University, London, ON, Canada, <sup>4</sup>Department of Clinical Neurological  
10                   Sciences, Schulich School of Medicine and Dentistry, Western University, London, ON, Canada,  
11                   <sup>5</sup>Department of Medical Imaging, Schulich School of Medicine and Dentistry, Western University,  
12                   London, ON, Canada, <sup>6</sup>Department of Medical Biophysics, Schulich School of Medicine and  
13                   Dentistry, Western University, London, ON, Canada, <sup>7</sup>Department of Psychology, Western  
14                   University, London, ON, Canada, <sup>8</sup>Department of Epidemiology and Biostatistics, Schulich  
15                   School of Medicine and Dentistry, Western University, London, ON, Canada. <sup>†</sup>Corresponding  
16                   author L.M., email: [lmuller2@uwo.ca](mailto:lmuller2@uwo.ca)

17  
18                   **Sleep is generally considered to be a state of large-scale synchrony across thalamus and**  
19                   **neocortex; however, recent work has challenged this idea by reporting isolated sleep**  
20                   **rhythms such as slow-oscillations and spindles. What is the spatial scale of sleep**  
21                   **rhythms? To answer this question, we adapted deep learning algorithms initially**  
22                   **developed for detecting earthquakes and gravitational waves in high-noise settings for**  
23                   **analysis of neural recordings in sleep. We then studied sleep spindles in non-human**  
24                   **primate ECoG, human EEG, and clinical intracranial recordings (iEEG) in the human. We**  
25                   **find a widespread extent of spindles, which has direct implications for the spatiotemporal**  
26                   **dynamics we have previously studied in spindle oscillations (Muller et al., 2016) and the**  
27                   **distribution of memory engrams in the primate.**

28  
29                   Consolidation of long-term memories requires precise coordination of pre- and post-synaptic  
30                   spikes across neocortex. New memories are transferred from hippocampus to neocortex for long-  
31                   term storage (McClelland et al., 1995; Rasch and Born, 2007), where interconnections within a  
32                   sparse, distributed neuron group are strengthened until their activity becomes hippocampus-  
33                   independent (Frankland and Bontempi, 2005). Computational studies have identified neural  
34                   oscillations as a potential mechanism to regulate synaptic plasticity (Masquelier et al., 2009; Song

35 et al., 2000) and create precise spike timing (Cassenaer and Laurent, 2007; Muller et al., 2011).  
36 Further, experiments have shown that the stage 2 sleep “spindle” oscillation influences spiking  
37 activity (Contreras and Steriade, 1995; Kandel and Buzsáki, 1997; Peyrache et al., 2011) and  
38 causally contributes to sleep-dependent consolidation of long-term memory (Mednick et al.,  
39 2013). It remains unclear, however, precisely how this rhythm can coordinate activity across areas  
40 in neocortex for synaptic plasticity and long-term storage to occur.

41  
42 While early recordings in anesthetized animals (Andersen et al., 1967; Contreras et al., 1996) and  
43 human EEG (Achermann and Borbély, 1998) indicated that sleep spindles generally occur across  
44 a wide area in cortex, creating a state of large-scale synchrony (Sejnowski and Destexhe, 2000;  
45 Steriade, 2003), recent work in intracranial recordings from human clinical patients has  
46 challenged this idea by reporting isolated, “local” sleep spindles (Andrillon et al., 2011; Nir et al.,  
47 2011; Piantoni et al., 2016; Sarasso et al., 2014, but see Frauscher et al., 2015). Because spindles  
48 are intrinsically related to sleep-dependent consolidation of long-term memory (Clemens et al.,  
49 2005; Gais et al., 2002; Mednick et al., 2013), this difference in reported spatial extent of the  
50 spindle raises an important question for the organization of engrams established through sleep-  
51 dependent memory consolidation. Recent evidence using *cFos* mapping in animal models  
52 suggests these engrams are distributed widely across brain areas (Kitamura et al., 2017; Roy et  
53 al., n.d.), which is consistent with previous imaging evidence in the human (Brodt and Gais, 2020;  
54 Wheeler et al., 2000). Taking these points together, we reasoned that widespread, multi-area  
55 spindles may occur more often than previously reported in primate and human cortex. If this were  
56 the case, these widespread spindles could provide the mechanism needed to link populations  
57 distributed widely across the cortex for sleep-dependent memory consolidation.

58  
59 Plasticity of long-range excitatory connections linking distant neuron groups occurs through spike-  
60 time dependent plasticity (STDP) (Bi and Poo, 1998; Markram et al., 1997), for which presynaptic  
61 vesicle release and postsynaptic spiking must occur with a precision of a few milliseconds (Magee  
62 and Johnston, 1997). Long-range synaptic connections in cortex result primarily from excitatory  
63 pyramidal neurons (Schüz and Braitenberg, 2002; Sholl, 1956), and these connections could  
64 provide a link among local networks representing pieces of a memory in different brain regions.  
65 The key missing piece is to understand how spindles can guide specific long-range excitatory  
66 connections to strengthen during sleep-dependent memory consolidation. We thus hypothesized  
67 that widespread, multi-area spindles might provide this mechanism.

68

69 Reliably detecting individual spindles in noisy sleep recordings, however, is challenging. Spindle  
70 oscillation amplitudes differ across regions in cortex (Frauscher et al., 2015). Furthermore,  
71 oscillation amplitudes may differ significantly across recording sites simply due to variation in  
72 electrode properties (Kappenman and Luck, 2010; Nelson and Pouget, 2010). For these reasons,  
73 we reasoned that fixed amplitude thresholds, which are a technique common across methods for  
74 spindle detection, may only detect the largest amplitude events, potentially leading to an  
75 underestimation of spatial extent. To address this question, we adapted deep learning algorithms  
76 initially developed for detecting earthquakes (Perol et al., 2018) and gravitational waves (George  
77 and Huerta, 2018) in high-noise settings to analysis of neural recordings in sleep. We studied  
78 sleep spindles in macaque non-human primate (NHP) electrocorticogram (ECoG), human  
79 electroencephalogram (EEG), and, finally, clinical intracranial electroencephalogram (iEEG)  
80 recordings, which provide a window into the circuits of the human brain at one of the highest  
81 spatial resolutions possible (Lachaux et al., 2012; Mukamel and Fried, 2012). Our approach,  
82 which detects a range of clearly formed large- and small-amplitude spindles during sleep, reveals  
83 that the spatial extent of spindles, defined here in terms of co-occurrence across electrode sites,  
84 is widely distributed over a broad range of cortex. In particular, multi-area spindles are much more  
85 frequent than previously estimated by amplitude-thresholding approaches, which tend to select  
86 only the highest-amplitude spindles and could miss events that transiently fall below threshold.  
87 Importantly, these results were additionally verified using a signal-to-noise ratio (SNR) approach  
88 (Muller et al., 2016), which is a conservative but approximately amplitude-invariant technique  
89 closely related to the constant false alarm rate (CFAR) method used in radar (Richards, 2005).  
90 Lastly, in human sleep EEG after low- and high-load visual working memory tasks, our method  
91 detects an increase in regional and multi-area spindles uniquely following a high-load visual  
92 memory task. Taken together, these results provide substantial evidence of a specific role for  
93 spindles in linking neuron groups distributed widely across cortex during memory consolidation.  
94

95 Sleep recordings from both human and NHP were obtained from electrodes ranging from the  
96 traditional scalp EEG to invasive intracranial EEG electrodes (Figure 1a). To verify the quality of  
97 spindles detected by our convolutional neural network (CNN) model (Figure 1c), we first compute  
98 average power spectral densities (PSDs) over spindle and non-spindle windows. The average  
99 PSD of detected spindle events shows an increase in the 11-15 Hz spindle frequency range (red  
100 lines, Figure 1b), while non-spindle events do not show a corresponding increase (black lines,  
101 Figure 1b). Spindles detected by the CNN are well-formed, consistent with standard morphology  
102 (Loomis et al., 1935; Newton Harvey et al., 1937; Silber et al., 2007) (Figure 1d), and in

103 agreement with previously observed durations ( $0.69 \pm 0.004$  seconds, NHP ECoG;  $0.87 \pm 0.006$   
104 seconds, EEG;  $0.74 \pm 0.003$  seconds, iEEG) (Fernandez and Lüthi, 2020; Takeuchi et al., 2016;  
105 Warby et al., 2014). To further validate spindles detected by the CNN, we designed a time-shifted  
106 averaging approach for application to recordings with only a 1 Hz highpass filter applied (thus  
107 excluding any potential effects from lowpass filtering). To do this, we collected signals from  
108 detected spindles, filtered at a 1 Hz highpass, time-aligned the events to the largest positive  
109 value within the detected window (corresponding to a positive oscillation peak), and then  
110 computed the average across aligned events. With this approach, the average over detected  
111 spindles exhibited clear 11-15 Hz oscillatory structure (black line, Supplementary Figure 1), while  
112 no oscillatory structure is observed when averaging over time-matched randomly selected non-  
113 spindle activity (dashed red line, Supplementary Figure 1). This result demonstrates that spindles  
114 detected by the CNN exhibit the correct structure even in a mostly raw, unprocessed signal with  
115 no lowpass filtering applied. Finally, we compared the amplitude distribution of spindles detected  
116 by the CNN and amplitude-thresholding (AT) approach. In the intracranial recordings (ECoG and  
117 iEEG), AT detects a subset of spindles that are significantly higher-amplitude than those  
118 detected by the CNN ( $p < 0.02$ , NHP ECoG recordings;  $p < 1 \times 10^{-14}$ ; iEEG recordings, one-sided  
119 Wilcoxon signed-rank test; n.s. in EEG), consistent with the expectation that AT will select the  
120 largest amplitude events. The CNN, however, can find well-formed spindles that are both large  
121 and small in amplitude (Supplementary Figure 2). This improved resolution allows us to study  
122 the spatial extent of spindles in an approximately amplitude-invariant manner.

123  
124 What is the spatial extent of spindle oscillations across cortex? To answer this question, we  
125 studied the distribution of simultaneously detected spindles across recording sites. We defined  
126 three classes of spindles based on co-occurrence across recording sites: local (1-2 sites), regional  
127 (3-10 sites), and multi-area (more than 10 sites). We noted our CNN approach detected many  
128 spindles with electrode sites distributed widely across the cortex (Figure 2a). By taking the unique  
129 cortical regions covered by the electrodes into account, we verified these were multi-area spindle  
130 events (Figure 2b). We then compared spindles detected by the CNN and AT approaches. To do  
131 this, we computed the ratio of spindles detected by the CNN and AT for all classes. This  
132 comparison revealed multi-area spindles were systematically detected approximately 1.5 (ECoG)  
133 to 10 (iEEG) times more often with the CNN than with the AT (Figure 2c and Supplementary  
134 Figure 3). Across all recordings, the increase in the multi-area spindles detected by the CNN was  
135 significantly greater than in the local spindles ( $p < 1 \times 10^{-3}$ , NHP ECoG recordings;  $p < 1 \times 10^{-6}$ ,  
136 EEG recordings;  $p < 0.02$ , iEEG recordings, one-sided Wilcoxon signed-rank test; similar results

137 for the local-regional comparison,  $p < 0.01$ , EEG recordings;  $p < 0.02$ , iEEG recordings, one-sided  
138 Wilcoxon signed-rank test, n.s. in NHP ECoG). Taken together, these results demonstrate that  
139 spindles appear much more widespread across cortex when detected using our approximately  
140 amplitude-invariant deep learning approach.

141

142 The organization of spindles across the cortex is thus neither fully local nor fully global: the co-  
143 occurrence patterns of this sleep rhythm contain a mixture of local and widespread events. If this  
144 is the case, what is the impact of the distribution on sleep-dependent memory consolidation? To  
145 answer this question, we further studied the human EEG dataset, which had the unique feature  
146 of testing sleep after tasks with varying memory loads. Briefly, before nap EEG recordings,  
147 subjects completed a task in which five novel outdoor scenes (high visual working memory, H-  
148 WM) or two novel outdoor scenes (low visual working memory, L-WM) were required to be held  
149 in working memory for six seconds (Figure 3a). After the delay period, subjects were then  
150 presented with a subsequent visual scene and asked whether it belonged to the previously  
151 presented set. In each case (H-WM and L-WM), trials were balanced so that the same total  
152 number of visual scenes was presented before sleep. An increase in spindle density after memory  
153 tasks and its relationship with memory consolidation is well established (Clemens et al., 2005;  
154 Dang-Vu et al., 2008; Gais et al., 2002; Schabus et al., 2007, 2004); however, the effect of  
155 memory tasks on co-occurrence remains unknown. Considering the potential circuit mechanism  
156 for spindles to link activity in neuron groups distributed across multiple areas in cortex through  
157 long-range excitatory connections (Muller et al., 2016), we then hypothesized sleep following  
158 high-load visual memory tasks would exhibit more multi-area spindles and a larger spatial extent.  
159 To test this hypothesis, we first confirmed that amplitudes of detected spindles did not differ across  
160 L-WM and H-WM conditions ( $p > 0.77$ , Wilcoxon signed-rank test). We then computed the rate of  
161 multi-area spindles after L-WM and H-WM tasks. Both regional and multi-area spindles appeared  
162 more often after H-WM than L-WM ( $p < 0.032$ , regional spindles;  $p < 0.006$ , multi-area spindles;  
163 one-sided paired-sample t-test) as detected by the CNN model, consistent with our hypothesis  
164 (Figure 3b). Similarly, the largest increases following H-WM versus L-WM were observed in the  
165 subset of regional and multi-area spindles detected by the more-conservative SNR approach  
166 (Supplementary Figure 4a); however, no increase in multi-area spindles was observed with the  
167 AT algorithm (Supplementary Figure 4b).

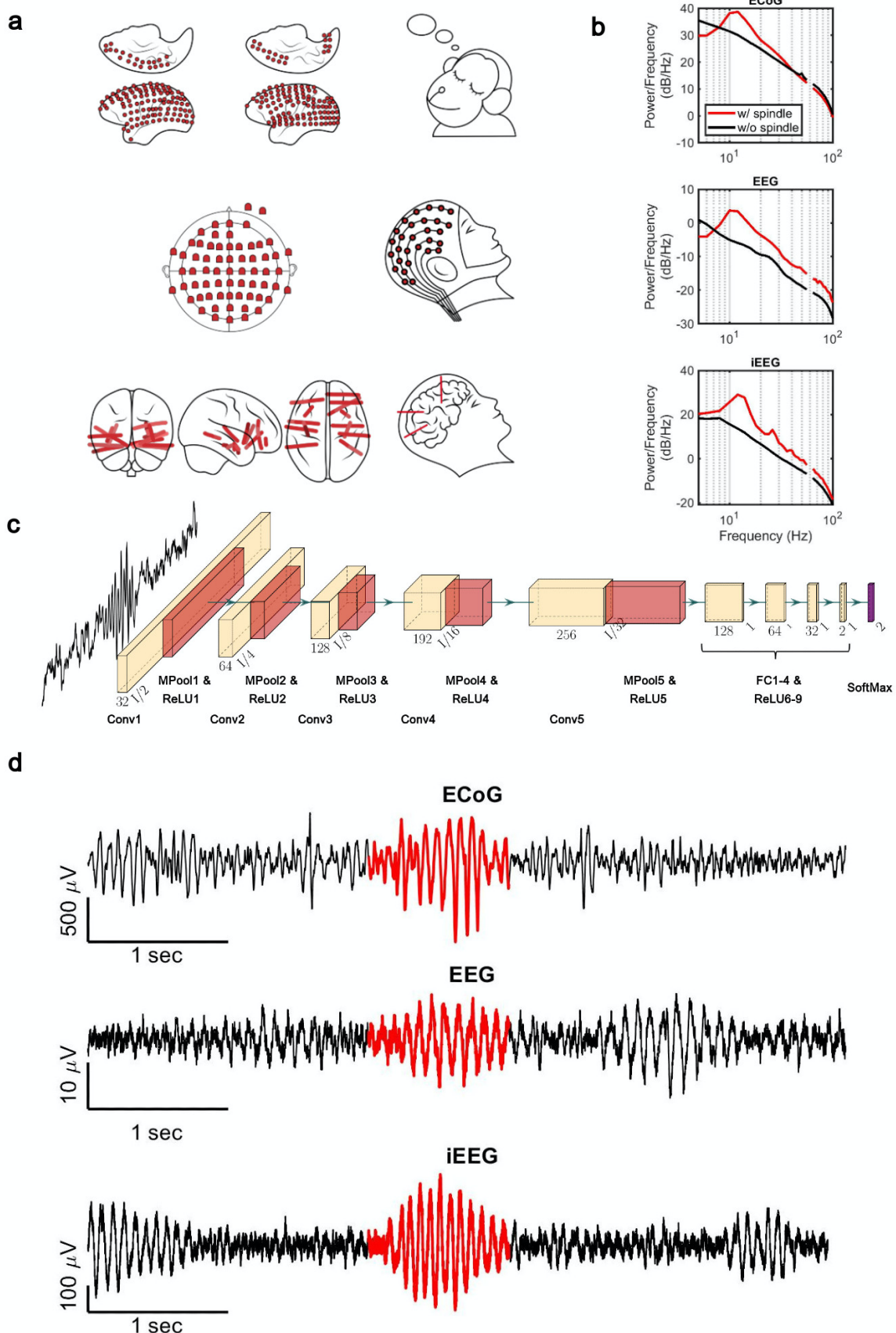
168

169 In this work, we have studied sleep spindles from human and NHP sleep recordings. To analyze  
170 these recordings, we adapted newly developed deep learning approaches for detecting rhythmic

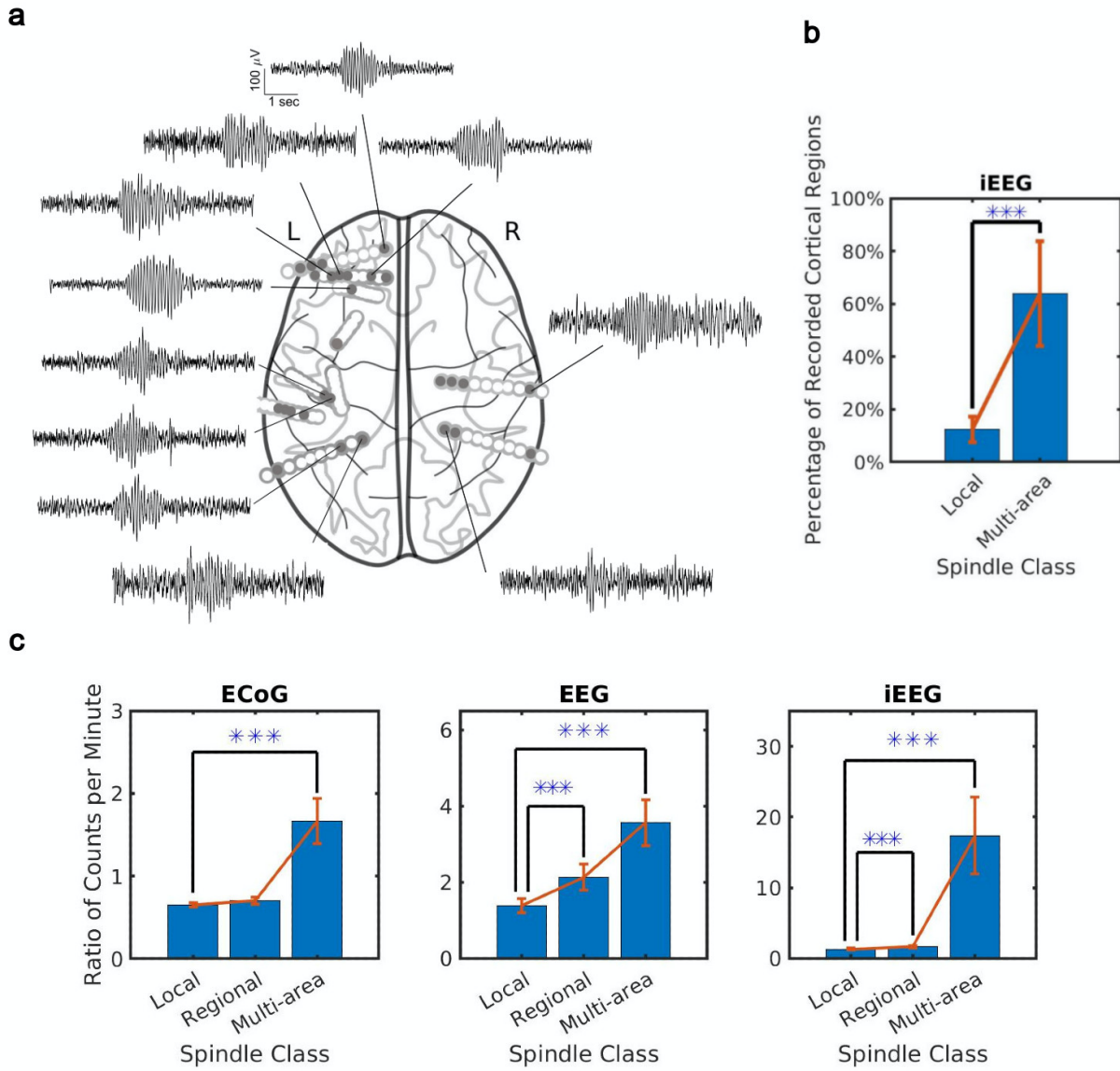
171 events in high-noise data (George and Huerta, 2018; Perol et al., 2018). We validated this  
172 approach through a series of control analyses and comparison to the subset of spindles detected  
173 by a similarly amplitude-invariant but more-conservative SNR algorithm. We found that large,  
174 multi-area spindles, where more than 10 electrode sites exhibit this rhythm simultaneously, are  
175 much more prevalent than previously estimated by amplitude-thresholding approaches (Andrillon  
176 et al., 2011; Nir et al., 2011; Piantoni et al., 2016; Sarasso et al., 2014), which tend to select only  
177 the highest-amplitude events.

178

179 While it has become increasingly clear that sleep spindles play an active and causal role in sleep-  
180 dependent memory consolidation (Aton et al., 2014; Clemens et al., 2005; Eschenko et al., 2006;  
181 Gais et al., 2002; Mednick et al., 2013; Rasch and Born, 2013), it remains unclear how these  
182 oscillations coordinate activity across areas to drive formation of strong neocortical assemblies  
183 distributed over long distances (Klinzing et al., 2019). Episodic memories often contain a detailed  
184 multisensory scene (Horner and Burgess, 2013; Tulving, 1983), and the activity patterns  
185 associated with these memories recruit distributed representations from association to primary  
186 sensory areas (Horner et al., 2015; Wheeler et al., 2000). In recent work, we found that sleep  
187 spindles can be organized into large-scale waves rotating across neocortex (Muller et al., 2016),  
188 and we hypothesized that these waves could provide a mechanism by which long-range excitatory  
189 connections between distant populations in cortex could be strengthened during memory  
190 consolidation in sleep. This potential mechanism for memory consolidation is interesting in light  
191 of recent research showing wide distribution of memory engrams (Kitamura et al., 2017; Roy et  
192 al., n.d.) and experience-dependent myelination formation in memory consolidation (Pan et al.,  
193 2020; Wang et al., 2020), both of which are consistent with the development of distributed  
194 assemblies across neocortex by these waves. In this work, by adapting deep learning algorithms  
195 for waveform detection in high-noise recordings (George and Huerta, 2018; Perol et al., 2018),  
196 we have found that large-scale, multi-area spindles occur much more often than previously  
197 reported. Following these observations, we then hypothesized that large, multi-area spindles  
198 exhibit an increase following high-load memory tasks. Consistent with this hypothesis, both the  
199 CNN and SNR methods detect an increase in multi-area spindles uniquely following high-load  
200 memory tasks. These results thus provide a specific neural mechanism by which memories can  
201 be stored in distributed neocortical networks during sleep.

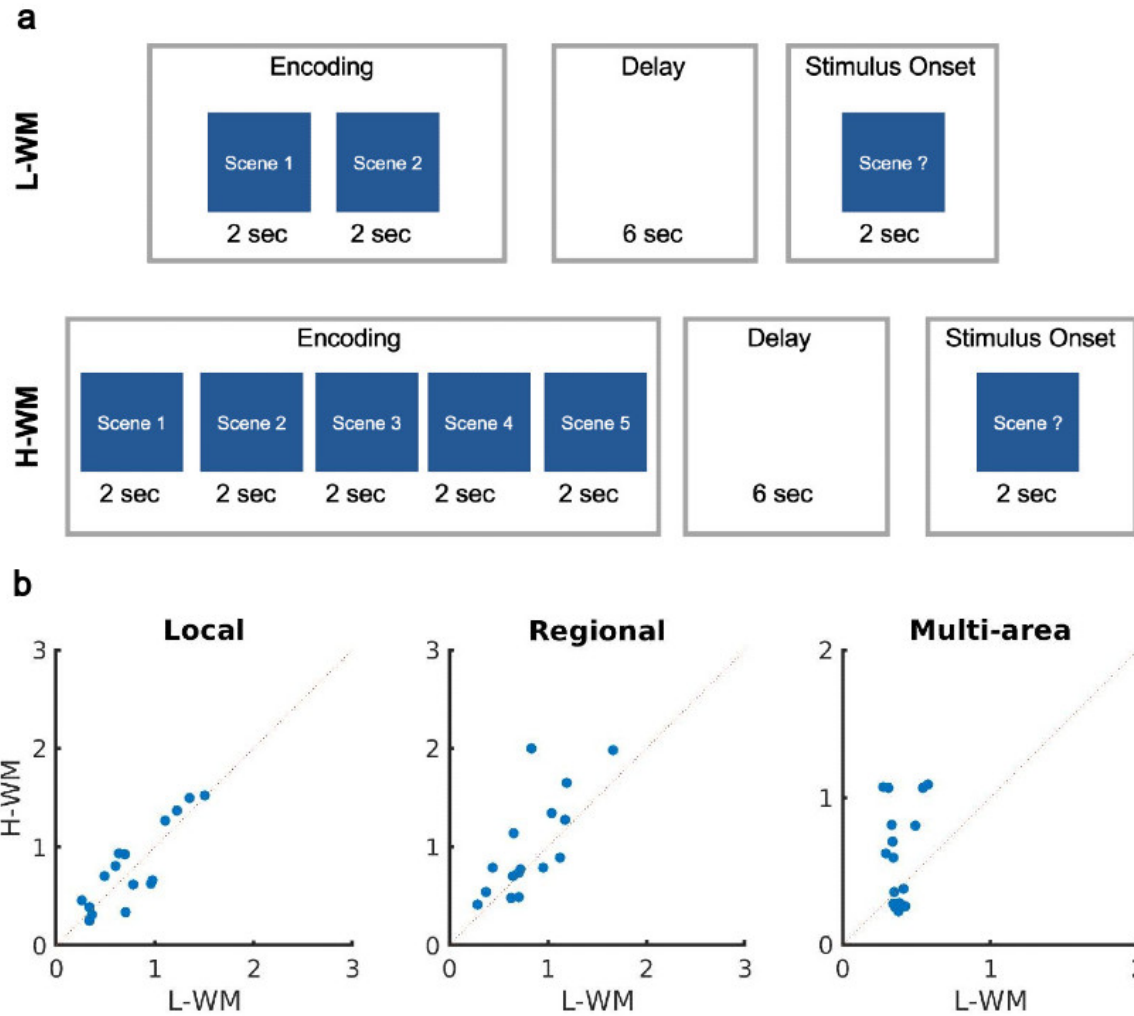


203 **Figure 1. (a)** Electrode placement of multichannel ECoG recordings of two macaques (**top**), high-  
204 density scalp EEG used for recordings after high and low visual memory tasks (**middle**), and  
205 example iEEG contacts in a human clinical patient (**bottom**). **(b)** Average power spectral density  
206 estimate for spindle windows detected by the CNN model (red) and matched non-spindle windows  
207 (black), illustrating the nearly 10 dB increase within the 11–15 Hz spindle band in NHP ECoG  
208 recordings (**top**), human EEG recordings (**middle**), and human iEEG recordings (**bottom**). Power  
209 at line noise frequency omitted for clarity. **(c)** The architecture of the CNN model developed for  
210 spindle detection. **(d)** Examples of detected spindles by the CNN model (red) in NHP ECoG  
211 recordings (**top**), human EEG recordings (**middle**), and human iEEG recordings (**bottom**).  
212



213

214 **Figure 2. Distribution of the extent of spindles detected by CNN and AT approaches.** (a) An  
215 example of a widespread, multi-area spindle with electrode sites distributed widely across the  
216 cortex. Filled gray circles indicate electrode contacts in gray matter. (b) Plotted is the percentage  
217 of unique recorded cortical regions with spindles detected by the CNN in the local versus multi-  
218 area case across all subjects in the iEEG recordings (average  $\pm$  SEM). (c) Plotted are the ratios  
219 of spindles detected by the CNN and AT in NHP ECoG recordings (left), human EEG recordings  
220 (middle), and iEEG recordings (right) in local (1-2 sites), regional (3-10 sites) and multi-area  
221 (more than 10 sites) spindle classes (average  $\pm$  SEM in all cases). Across recordings, the increase  
222 in regional and multi-area spindles detected by the CNN is significantly larger than for the local  
223 spindles (except local vs. regional in the NHP ECoG).



224

225 **Figure 3. Impact of visual memory load on sleep spindle occurrence. (a)** Schematic  
226 representation of low and high visual working memory tasks. **(b)** Average number of spindles  
227 detected per minute in high versus low visual working memory condition. Spindles are grouped  
228 into local (**left**), regional (**middle**) and multi-area (**right**) classes detected by the CNN model. A  
229 significant increase in the number of spindles among subjects can be observed in multi-area and  
230 regional spindles as opposed to local spindles ( $p > 0.34$ , local spindles;  $p < 0.032$ , regional  
231 spindles;  $p < 0.006$ , multi-area spindles; one-sided Wilcoxon signed-rank test).

232

233

234

235

236

## Methods

237

238 **Recordings.** We study performance of the CNN model across three sleep datasets obtained from  
239 electrodes ranging from traditional scalp EEG to invasive intracranial depth electrodes. These  
240 datasets represent recordings from very different electrode types, which vary widely in resolution  
241 and signal-to-noise ratio. Training the CNN model in the same way over these very different  
242 recordings demonstrates the generality of the framework developed here; further, these results  
243 also represent a cross-species comparison of sleep-rhythm dynamics in NHP and human  
244 neocortex.

245

246 The first dataset contains electrocorticographic (ECoG) recording from most of the lateral cortex  
247 in two macaques during natural sleeping conditions (Yanagawa et al., 2013). Recordings were  
248 obtained from 128 electrodes in both monkeys and sampled at 1 kHz by a Cerebus data  
249 acquisition system (Blackrock Microsystems, Salt Lake City, UT, USA). The quality of sleep was  
250 studied by the degree of spatial synchronization in slow wave oscillations and significant increase  
251 in delta power was reported in sleep condition versus waking activity. This dataset was recorded  
252 and distributed by Laboratory for Adaptive Intelligence, BSI, RIKEN and was made freely available  
253 at <http://neurotycho.org/sleep-task>.

254

255 The second dataset contains high-density scalp electroencephalography (EEG) recording from  
256 20 healthy participants (Mei et al., 2018). Each participant participated in two separate sessions  
257 and completed a high- and low-load visual working memory task. The recordings were obtained  
258 during naps following the working memory tasks from a 64-electrode EEG skull cap and sampled  
259 at 1 kHz. The recordings were reviewed and stage 2 sleep was manually annotated by an expert  
260 to verify quality of sleep recordings. Ultimately, sleep recordings that did not reach stage 2 sleep  
261 or were too noisy were excluded from the study. Under these criteria, four subjects were excluded  
262 (subject 12, 20, 26 and 27). In addition, the recordings were common average referenced (CAR)  
263 to remove large artifacts with potentially non-neural origin. These recordings were made freely  
264 available at the Open Science Framework through the link <https://osf.io/chav7>.

265

266 The last dataset contains intracranial electroencephalography (iEEG) recordings from 5 epileptic  
267 patients in the Epilepsy Monitoring Unit (EMU) at London Health Sciences Centre (LHSC).  
268 Patients were implanted using depth electrodes for the sole purpose of surgical evaluation.  
269 Informed consent was collected from the patients in accordance with local Research Ethics Board

270 (REB) guidelines. Each patient was implanted with 9 to 14 iEEG electrodes located across the  
271 cortex with up to 10 contacts in gray or white matter (Supplementary Table 1). The iEEG signals  
272 were recorded continuously for a duration of 7 to 14 days for the purpose of seizure localization.  
273 We use clinically annotated sleep onsets and study half an hour recording starting from the  
274 beginning of the sleep/nap cycles in electrode contacts located within gray matter.

275

276 **Signal-to-noise ratio (SNR) measure for sleep spindle detection.** To specify a subset of  
277 spindles required to train our convolutional neural network (CNN) model, we implemented a  
278 modified version of signal-to-noise ratio (SNR) algorithm (Muller et al., 2016). This algorithm,  
279 which is inspired by the adaptive, constant-false-alarm-rate (CFAR) technique in radar, was used  
280 to detect narrow-band rhythmic activities. We measure the ratio of power within the frequency  
281 band of interest (here, 9-18 Hz) to power in the rest of the spectrum (1-100 Hz bandpass, with  
282 band-stop at 9-18 Hz) at each electrode. The SNR measure is computed over a sliding window  
283 of time (500 ms) and produces an estimate of how power in the frequency band of interest  
284 compares to total power in the recording, taking into account the noise on individual electrodes.  
285 We then used the SNR algorithm to produce high-quality training samples for the CNN model. To  
286 do this, we reduced the probability of false positives by setting the threshold to the 99<sup>th</sup> percentile  
287 of the SNR distribution, thus detecting only the activity patterns that have the highest unique  
288 power concentration in the spindle frequency range. We additionally required the SNR algorithm  
289 to only include activities with a duration between 0.5 to 3 seconds, consistent with the duration of  
290 sleep spindles. The detected windows are then used for training the CNN model.

291

292 To additionally verify performance of the SNR algorithm, we implement this approach over one  
293 second recordings of a 90 by 90 array of LFPs generated by a spiking network model of cortical  
294 activity in the awake state, which does not contain the thalamic reticular loops and thalamocortical  
295 projections needed to generate sleep spindles. SNR values calculated from these data were  
296 uniformly below 0 dB, confirming the robustness of our approach in uniquely detecting spindle-  
297 frequency activity through a known ground truth dataset.

298

299 **Convolutional neural network (CNN) for sleep spindle detection.** We developed a  
300 convolutional neural network (CNN) to detect spindles activities during sleep. The model is  
301 motivated by the successful implementation of deep learning for detecting earthquakes and  
302 gravitational waves in high-noise settings (George and Huerta, 2018; Perol et al., 2018). If trained  
303 properly, it has the ability to detect hidden spindles that are being unnoticed and provides a great

304 opportunity to study the spatial and temporal analysis of spindle activities across the cortex. We  
305 first tested CNN models with different architectures and selected one of the best architectures  
306 across the sleep recording datasets (Figure 1c). Our CNN model is a one dimensional model with  
307 5 convolutional layers (with 32, 64, 128, 192 and 256 filters) and 4 fully connected layers (with  
308 sizes 128, 64, 32 and 2). Each convolutional layer is followed by a maxpool and rectified linear  
309 unit layers and the output of the fifth convolutional layer is gradually flattened into 2D vectors  
310 using the fully connected layers followed by rectified linear unit layers. Our classifier has an  
311 additional softmax layer at the end which returns the probability of spindle in addition to the  
312 predicted label. The CNN model takes a window of sleep recording (500 ms which is bandpass  
313 filtered at 1-100 Hz after removal of line noise and harmonics) as an input and predicts its label  
314 (spindle or non-spindle). The hyperparameters of the CNN model are optimized to minimize the  
315 difference in the predicted and actual labels determined by the SNR algorithm.

316

317 **Power-spectral density estimate.** To verify performance of the CNN, SNR and AT approaches,  
318 we compared power spectral density (PSD) estimates of spindle and non-spindle activities  
319 (Welch's method; Figure 1b and Supplementary Figure 5). In both cases, we first remove line  
320 noise artifacts. We then compute PSD over windows of 0.5 s with no overlap and average spectra  
321 over detected events. Matched non-spindle PSDs were estimated over a large number of  
322 randomly selected non-spindle windows. The increase in the power during the natural frequency  
323 range of sleep (~9-18 Hz) in spindle vs non-spindles activities demonstrates the ability of both the  
324 CNN model and SNR algorithm to correctly identify spindle activities.

325

326 **Time-shifted averaging control.** As an additional control analysis, we computed average signals  
327 over detected spindles, with activity shifted to align the largest oscillation peak in the detected  
328 time window. To compute this average, we first needed to correct for the time offset between  
329 different spindles. To do this, we shifted detected spindles to the largest positive value within the  
330 detected window, corresponding to the positive potential of an individual spindle oscillation cycle,  
331 and then took the average over all time-shifted windows. The average of time-shifted signals is  
332 computed over spindle windows detected by the CNN approach, as well as matched randomly  
333 selected non-spindle windows. Importantly, while the time-shifted average clearly exhibits 11-15  
334 Hz oscillatory structure when computed over spindle events detected by the CNN, this need not  
335 be the case, as demonstrated by application of the same approach to matched non-spindle events  
336 (Supplementary Figure 1).

337

338 We also systematically studied the sensitivity of the CNN model as a function of the SNR threshold  
339 used for building the training set. To do this, we computed the time-shifted average over spindle  
340 events detected by the CNN model at different levels of the SNR threshold (Supplementary Figure  
341 6). Clear, well-formed 11-15 Hz oscillatory structure is observed in the time-shifted averages  
342 above 0 dB threshold, verifying the quality of detected spindles by the corresponding CNN  
343 models. However, the 11-15 Hz oscillatory structure starts to disappear below 0 dB because an  
344 SNR threshold below 0 dB introduces errors into the training sets by mislabeling noise signals as  
345 spindles. On the other hand, similar oscillatory shapes of time-shifted average above 0 dB  
346 confirms the ability of the CNN model to perform robustly while trained over different sets of  
347 clearly-formed spindles.

348

349 **Comparison with amplitude-threshold approach.** The amplitude threshold (AT) approach has  
350 been used extensively in the literature to automatically detect spindles during sleep(Gais et al.,  
351 2002; Nir et al., 2011). In this approach, a spindle is detected when the amplitude of the bandpass  
352 signal stays above a threshold for a limited period of time (e.g. at least 500 ms; cf. Supplementary  
353 Figure 5 in Nir et al., 2011). To implement this approach, we first bandpass filter the signal at the  
354 frequency of 11-15 Hz and then compute the root mean square (RMS) of its amplitude over a  
355 sliding window of 0.5 seconds. A spindle is detected whenever the RMS amplitude stays above  
356 the predetermined threshold for 0.5 to 3 s. To determine the most appropriate threshold for  
357 comparison to the CNN and SNR approaches, we first computed the distribution of electrode-  
358 level RMS amplitude that results in approximately 2 spindles per minute and then set the overall  
359 threshold to its average across all electrodes. The quality and extent of detected spindles by the  
360 AT approach was then compared with the CNN and SNR (Figure 2c, Supplementary Figure 2, 3,  
361 4, 5 and 7). The CNN model has a relatively amplitude-invariant nature in comparison with the  
362 amplitude-thresholding (AT) approach, which is highly sensitive to a predefined cutoff amplitude  
363 threshold. The AT approaches may only select spindles with the largest-amplitude events, or  
364 could miss ones that temporarily dip below the threshold while our approach has the ability to find  
365 well-formed spindles that are both large- and small-amplitude (Supplementary Figure 2).

366

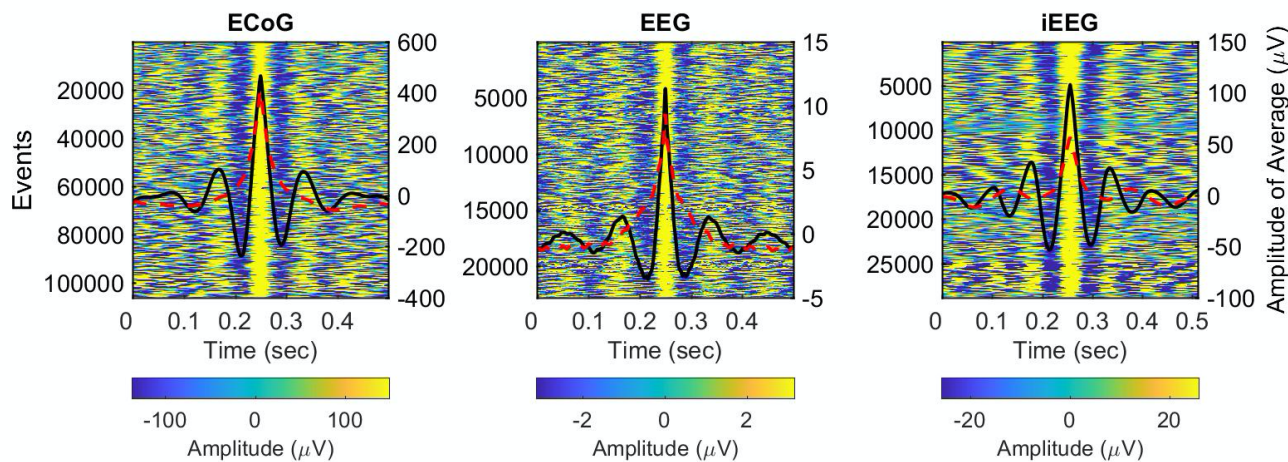
367 **Electrode Localization.** For the purpose of electrode localization in the iEEG recordings, we  
368 developed an image processing pipeline which involves electrode contact localization, brain  
369 tissue segmentation and atlas fitting. Semi-automatic contact localization was performed in  
370 3D Slicer using the SEEG Assistant module (Narizzano et al., 2017). The entry and target  
371 points of each electrode were manually defined on the post-operative CT image. The

372 entry/target labels were provided to the SEEGA algorithm, which automatically segmented  
373 the electrode contacts. To obtain brain location information for each contact, brain tissue  
374 segmentation and atlas fitting was carried out. To enable the use of anatomical priors during  
375 tissue segmentation, the pre-operative T1w MRI was non-linearly registered to the MNI152  
376 2009c Nonlinear Symmetric template  
377 (<https://www.bic.mni.mcgill.ca/ServicesAtlases/ICBM152NLin2009>) using NiftyReg (Modat et  
378 al., 2010). An anatomical mask was generated by applying the inverse transform to the T1w  
379 image using the antsApplyTransforms algorithm from Advanced Normalization Tools 2.2.0  
380 (ANTS; <http://stnava.github.io/ANTS>). Segmentation of gray matter, white matter, and  
381 cerebrospinal fluid was performed using the Atropos algorithm from ANTS(Avants et al.,  
382 2011b), which implements k-means classification (k=3). The resulting posteriors were merged  
383 into a 4D volume using the fslmerge algorithm from FMRIB Software Library v6.0 (FSL;  
384 <https://fsl.fmrib.ox.ac.uk/fsl/fslwiki>). The CerebrA atlas (Manera et al., 2020) was used to  
385 obtain anatomical labels for each electrode contact. Normalization to template space  
386 (MNI152NLin2009cAsym) was performed using the non-linear SyN (Avants et al., 2011a)  
387 symmetric diffeomorphic image registration algorithm from ANTS, using both the brain masks  
388 of the pre-operative T1w and template space. Using the inverse of the non-linear transform,  
389 the CerebraA atlas labels were warped to the pre-operative T1w MRI space. The atlas labels  
390 were then dilated using the fslmaths algorithm from FSL. The final T1w brain tissue/atlas  
391 segmentation was mapped to the contacts to provide location information for each contact  
392 (tissue probability and brain anatomical region). This custom processing pipeline has been  
393 made available on GitHub (<https://github.com/akhanf/clinical-atlasreg>).  
394

395 **Code availability.** Our custom MATLAB (MathWorks) implementations of all computational  
396 analyses, along with the analysis scripts used for this study will be made available as an open-  
397 access release on GitHub (<http://mullerlab.github.io>).

398

### Supplementary Figures



399

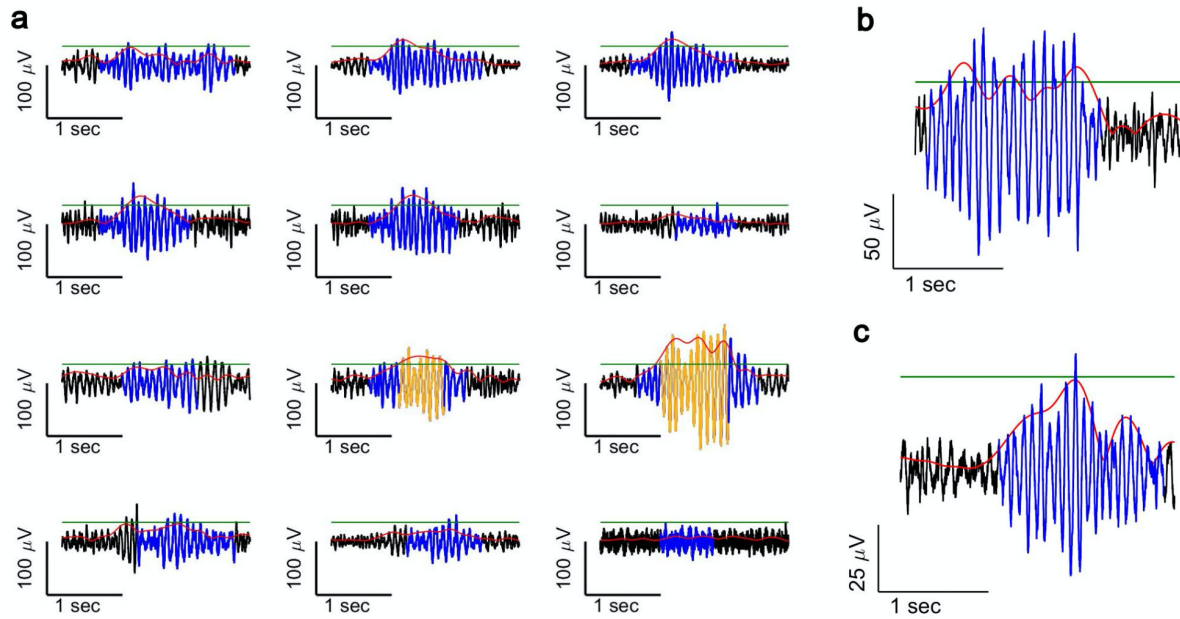
#### 400 **Supplementary Figure 1. Average time-shifted spindles detected by the CNN model.**

401 Examples of average signals computed over spindle windows detected by the CNN models (solid  
402 black lines) vs a subset of randomly matched non-spindle windows (dashed red lines) in NHP  
403 ECoG recordings (**left**), human EEG recordings (**middle**), and iEEG recordings (**right**). The  
404 average over detected spindle windows exhibits clear 11-15 Hz oscillatory structure, while no  
405 oscillatory structure is present in the average over matched non-spindle windows. The heatmaps  
406 in the background are the individual time-shifted spindle events, which demonstrate the presence  
407 of this structure in individual instances.

408

409

410

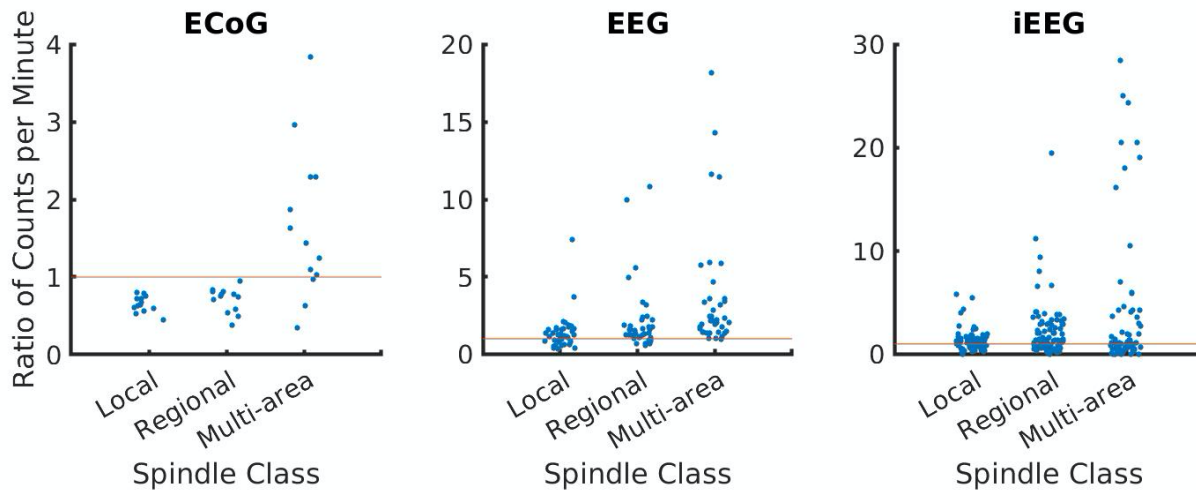


411

412 **Supplementary Figure 2. Performance of CNN model versus AT Algorithm.** (a) An example  
413 of co-occurring spindles detected by the CNN model in 11 sites. The red line is the root mean  
414 square amplitude of the signal, the green line is the amplitude threshold, and the blue line  
415 represents windows of time in which spindles were detected by the CNN model. The AT algorithm,  
416 which only detects spindle activities with amplitude above a predefined amplitude threshold for at  
417 least a duration of 0.5 sec (Nir et al., 2011) (yellow line), was not successful in detecting the  
418 majority of spindles in this example. Specifically, the AT algorithm fails to detect well-shaped  
419 spindles (detected by the CNN model) whose amplitudes temporarily drop below threshold (b) or  
420 have low amplitude (c).

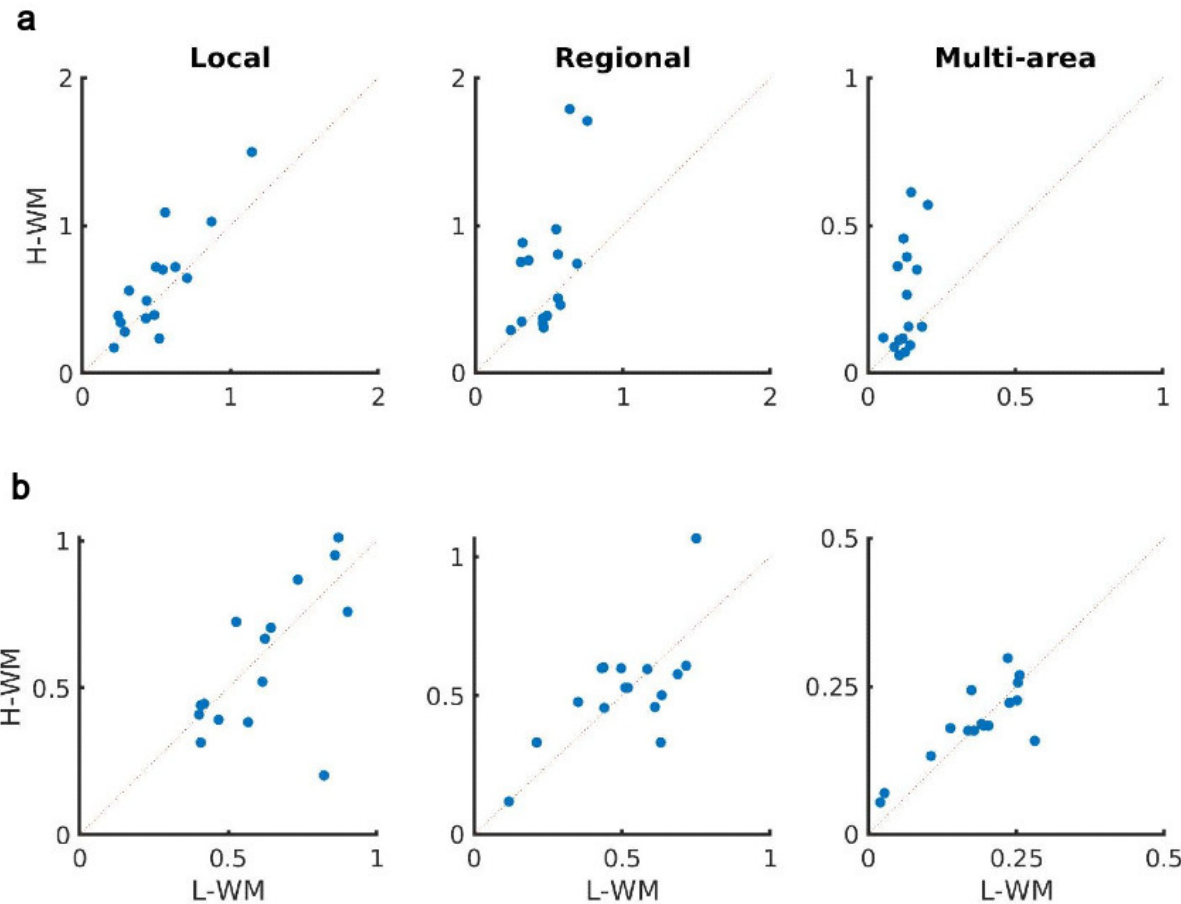
421

422



423

424 **Supplementary Figure 3. Distribution of the extent of spindles detected by CNN and AT**  
425 **approaches.** Plotted is the scatter diagram of the ratio of average number of detected spindles  
426 by the CNN and AT in NHP ECoG recordings (**left**), human EEG recordings (**middle**), and iEEG  
427 recordings (**right**) grouped into local (1-2 sites), regional (3-10 sites), and multi-area (more than  
428 10 sites) spindle classes. Each blue dot represents the ratio of the number of spindles per minute  
429 in one sleep recording.

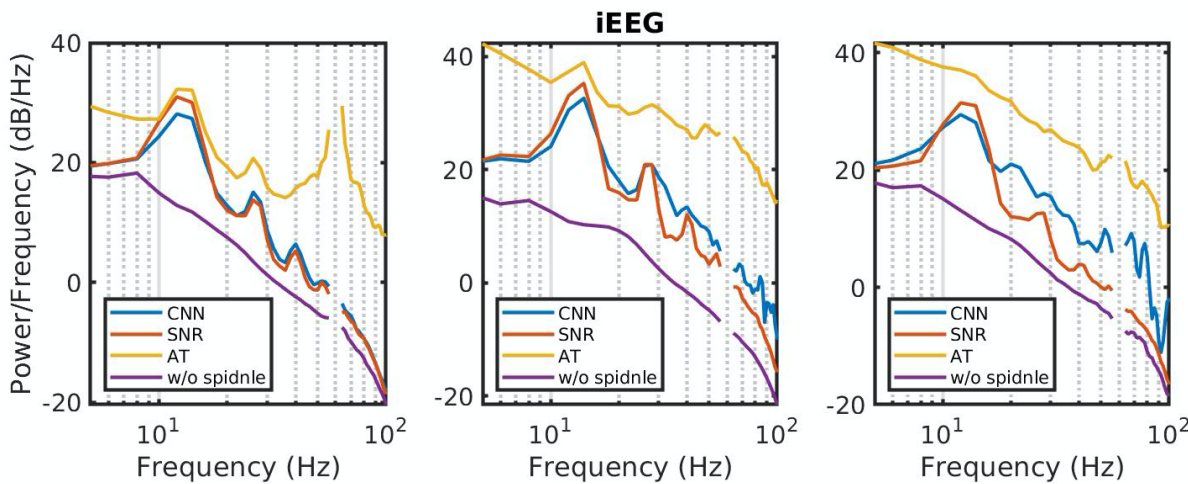


430

431 **Supplementary Figure 4. Low and high visual memory task and its impact on sleep spindle**  
432 **occurrence - SNR and AT.** (a) Average number of spindles detected per minute in high vs low  
433 visual working memory condition by the SNR. The SNR algorithm detected a significant increase  
434 in the number of spindles across subjects ( $p < 0.04$ , local spindles;  $p < 0.02$ , regional spindles;  $p$   
435  $< 0.007$ , multi-area spindles; one-sided paired-sample t-test), with the largest increases for  
436 regional and multi-area spindles. (b) Average number of spindles detected per minute in high vs  
437 low visual working memory condition by the AT. In contrast to the CNN, AT was not able to detect  
438 any significant increase in the number of distributed spindles among subjects across all spindles  
439 classes ( $p > 0.56$ , local spindles;  $p > 0.34$ , regional spindles;  $p > 0.30$ , multi-area spindles; one-  
440 sided paired-sample t-test).

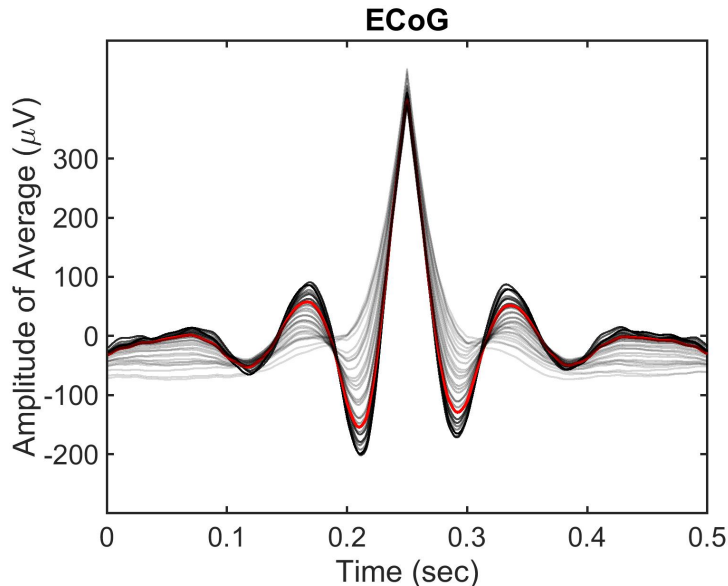
441

442

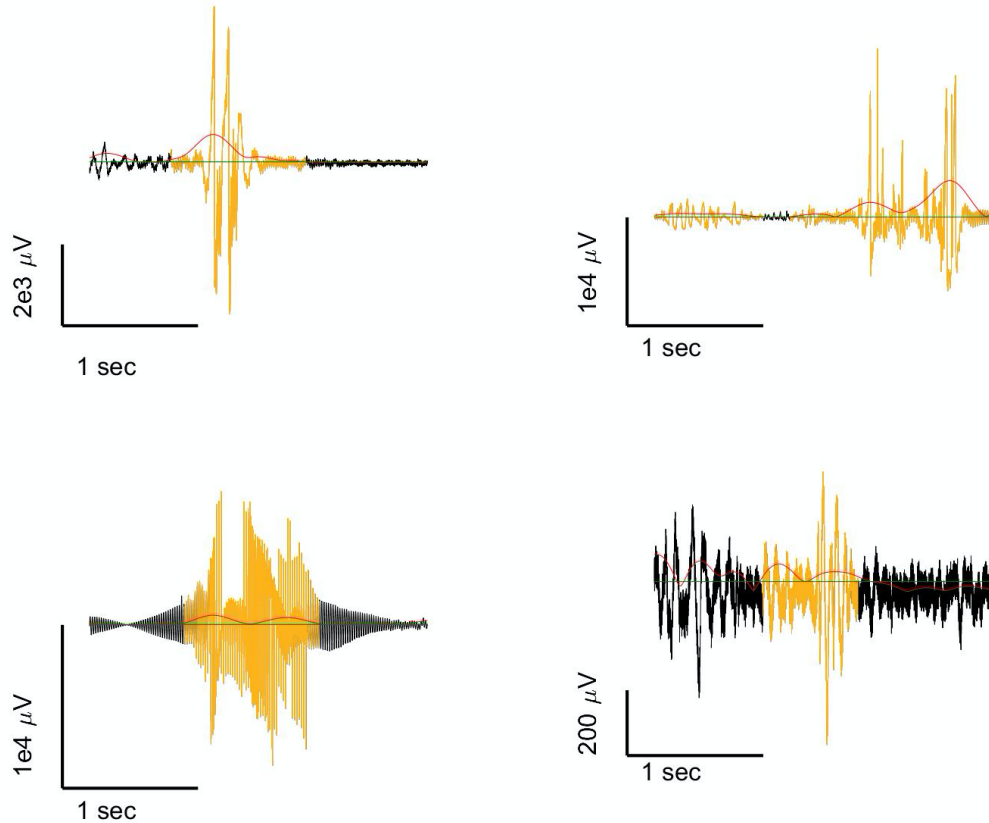


443 **Supplementary Figure 5. Power spectral density (PSD) comparison.** Examples of average  
444 power spectral density estimate over spindle windows detected by the CNN model (blue), the  
445 SNR approach (red), the AT algorithm (yellow) and matched non-spindle windows (purple) in  
446 iEEG recordings. The CNN and SNR PSDs exhibit a nearly 10 dB increase within the 11–15 Hz  
447 spindle band compared to matched non-spindle windows, while the AT PSD exhibits higher power  
448 outside of the frequency of interest in addition to spindle band. Power at line noise frequency  
449 omitted for clarity.

451



452  
453 **Supplementary Figure 6. Impact of SNR threshold on the CNN model.** Plotted is the change  
454 in the average time-shifted spindle detected by CNN models trained over a wide range of SNR  
455 thresholds (5 to -10 dB, dark to light gray) in the NHP ECoG recordings. Clearly detected spindle  
456 activity decreases with the SNR threshold, demonstrating that the CNN result breaks down when  
457 the model is trained on lower quality examples. The red line represents the average computed at  
458 0 dB threshold (which represents parity between power in the spindle passband and the rest of  
459 the signal spectrum), below which the average detected spindle activities starts to drift away from  
460 the expected 11-15 Hz oscillatory structure.



461  
462 **Supplementary Figure 7. Non-spindle activities detected by the AT algorithm.** Sleep  
463 recordings are subjected to artifacts, such as line noise, electrical noise, and movement artifacts  
464 that introduce signal distortion. These artifacts can result in false spindle activity detection in the  
465 AT approach. For example, the sharp artifact when filtered at 11–15 Hz in the AT approach  
466 appears as an oscillation which does not exist in the original recording (**top row**), or the AT  
467 approach might detect non-spindle activities resulting from broken channels (**bottom left**) or not  
468 clearly formed spindles (**bottom right**).

469  
470  
471  
472  
473  
474  
475

476 **Supplementary Table 1: Distribution of gray matter contacts in the cortical regions of all**  
477 **subjects in the iEEG recordings.**  
478

Brain Region	Subject A	Subject B	Subject C	Subject D	Subject E
Amygdala	0	5	4	4	0
Caudal Middle Frontal	0	0	0	0	3
Entorhinal	0	1	0	0	0
Fusiform	0	1	0	3	0
Hippocampus	8	12	8	6	0
Inferior Lateral Ventricle	0	0	2	0	0
Insula	1	27	17	1	9
Lateral Orbitofrontal	0	3	2	0	6
Lateral Ventricle	1	1	0	0	0
Medial Orbitofrontal	1	1	1	0	2
Middle Temporal	3	4	8	9	0
Pars Opercularis	0	0	1	0	0
Pars Orbitalis	0	1	0	0	0
Pars Triangularis	1	1	2	0	4
Rostral Anterior Cingulate	1	2	1	0	4
Rostral Middle Frontal	7	2	6	0	9
Superior Frontal	1	0	4	0	17
Superior Temporal	4	0	0	2	0
Transverse Temporal	0	0	0	1	0

479

480

481

482

483 **References**

- 484 Achermann P, Borbély AA. 1998. Coherence analysis of the human sleep  
485 electroencephalogram. *Neuroscience* **85**:1195–1208.
- 486 Andersen P, Andersson SA, Lømo T. 1967. Nature of thalamo-cortical relations during  
487 spontaneous barbiturate spindle activity. *J Physiol* **192**:283–307.
- 488 Andrillon T, Nir Y, Staba RJ, Ferrarelli F, Cirelli C, Tononi G, Fried I. 2011. Sleep spindles in  
489 humans: insights from intracranial EEG and unit recordings. *J Neurosci* **31**:17821–17834.
- 490 Aton SJ, Suresh A, Broussard C, Frank MG. 2014. Sleep promotes cortical response  
491 potentiation following visual experience. *Sleep* **37**:1163–1170.
- 492 Avants BB, Tustison NJ, Song G, Cook PA, Klein A, Gee JC. 2011a. A reproducible evaluation  
493 of ANTs similarity metric performance in brain image registration. *Neuroimage* **54**:2033–  
494 2044.
- 495 Avants BB, Tustison NJ, Wu J, Cook PA, Gee JC. 2011b. An open source multivariate  
496 framework for n-tissue segmentation with evaluation on public data. *Neuroinformatics*  
497 **9**:381–400.
- 498 Bi GQ, Poo MM. 1998. Synaptic modifications in cultured hippocampal neurons: dependence on  
499 spike timing, synaptic strength, and postsynaptic cell type. *J Neurosci* **18**:10464–10472.
- 500 Brodt S, Gais S. 2020. Memory Engrams in the Neocortex. *Neuroscientist* 1073858420941528.
- 501 Cassenaer S, Laurent G. 2007. Hebbian STDP in mushroom bodies facilitates the synchronous  
502 flow of olfactory information in locusts. *Nature* **448**:709–713.
- 503 Clemens Z, Fabó D, Halász P. 2005. Overnight verbal memory retention correlates with the  
504 number of sleep spindles. *Neuroscience* **132**:529–535.
- 505 Contreras D, Destexhe A, Sejnowski TJ, Steriade M. 1996. Control of spatiotemporal coherence  
506 of a thalamic oscillation by corticothalamic feedback. *Science* **274**:771–774.
- 507 Contreras D, Steriade M. 1995. Cellular basis of EEG slow rhythms: a study of dynamic  
508 corticothalamic relationships. *J Neurosci* **15**:604–622.
- 509 Dang-Vu TT, Schabus M, Desseilles M, Albouy G, Boly M, Darsaud A, Gais S, Rauchs G,  
510 Sterpenich V, Vandewalle G, Carrier J, Moonen G, Balteau E, Degueldre C, Luxen A,  
511 Phillips C, Maquet P. 2008. Spontaneous neural activity during human slow wave sleep.  
512 *Proc Natl Acad Sci U S A* **105**:15160–15165.
- 513 Eschenko O, Mölle M, Born J, Sara SJ. 2006. Elevated sleep spindle density after learning or  
514 after retrieval in rats. *J Neurosci* **26**:12914–12920.
- 515 Fernandez LMJ, Lüthi A. 2020. Sleep Spindles: Mechanisms and Functions. *Physiol Rev*  
516 **100**:805–868.
- 517 Frankland PW, Bontempi B. 2005. The organization of recent and remote memories. *Nat Rev  
518 Neurosci* **6**:119–130.
- 519 Frauscher B, von Ellenrieder N, Dubeau F, Gotman J. 2015. Scalp spindles are associated with  
520 widespread intracranial activity with unexpectedly low synchrony. *Neuroimage* **105**:1–12.
- 521 Gais S, Mölle M, Helms K, Born J. 2002. Learning-dependent increases in sleep spindle  
522 density. *J Neurosci* **22**:6830–6834.
- 523 George D, Huerta EA. 2018. Deep Learning for real-time gravitational wave detection and  
524 parameter estimation: Results with Advanced LIGO data. *Phys Lett B* **778**:64–70.
- 525 Horner AJ, Bisby JA, Bush D, Lin W-J, Burgess N. 2015. Evidence for holistic episodic  
526 recollection via hippocampal pattern completion. *Nat Commun* **6**:7462.
- 527 Horner AJ, Burgess N. 2013. The associative structure of memory for multi-element events. *J  
528 Exp Psychol Gen* **142**:1370–1383.
- 529 Kandel A, Buzsáki G. 1997. Cellular–Synaptic Generation of Sleep Spindles, Spike-and-Wave  
530 Discharges, and Evoked Thalamocortical Responses in the Neocortex of the Rat. *J  
531 Neurosci* **17**:6783–6797.

- 532 Kappenman ES, Luck SJ. 2010. The effects of electrode impedance on data quality and  
533 statistical significance in ERP recordings. *Psychophysiology* **47**:888–904.
- 534 Kitamura T, Ogawa SK, Roy DS, Okuyama T, Morrissey MD, Smith LM, Redondo RL,  
535 Tonegawa S. 2017. Engrams and circuits crucial for systems consolidation of a memory.  
536 *Science* **356**:73–78.
- 537 Klinzing JG, Niethard N, Born J. 2019. Mechanisms of systems memory consolidation during  
538 sleep. *Nature Neuroscience*. doi:10.1038/s41593-019-0467-3
- 539 Lachaux J-P, Axmacher N, Mormann F, Halgren E, Crone NE. 2012. High-frequency neural  
540 activity and human cognition: past, present and possible future of intracranial EEG  
541 research. *Prog Neurobiol* **98**:279–301.
- 542 Loomis AL, Harvey EN, Hobart G. 1935. POTENTIAL RHYTHMS OF THE CEREBRAL  
543 CORTEX DURING SLEEP. *Science* **81**:597–598.
- 544 Magee JC, Johnston D. 1997. A synaptically controlled, associative signal for Hebbian plasticity  
545 in hippocampal neurons. *Science* **275**:209–213.
- 546 Manera AL, Dadar M, Fonov V, Collins DL. 2020. CerebrA, registration and manual label  
547 correction of Mindboggle-101 atlas for MNI-ICBM152 template. *Sci Data* **7**:237.
- 548 Markram H, Lübke J, Frotscher M, Sakmann B. 1997. Regulation of synaptic efficacy by  
549 coincidence of postsynaptic APs and EPSPs. *Science* **275**:213–215.
- 550 Masquelier T, Hugues E, Deco G, Thorpe SJ. 2009. Oscillations, phase-of-firing coding, and  
551 spike timing-dependent plasticity: an efficient learning scheme. *J Neurosci* **29**:13484–  
552 13493.
- 553 McClelland JL, McNaughton BL, O'Reilly RC. 1995. Why there are complementary learning  
554 systems in the hippocampus and neocortex: insights from the successes and failures of  
555 connectionist models of learning and memory. *Psychol Rev* **102**:419–457.
- 556 Mednick SC, McDevitt EA, Walsh JK, Wamsley E, Paulus M, Kanady JC, Drummond SPA.  
557 2013. The critical role of sleep spindles in hippocampal-dependent memory: a  
558 pharmacology study. *J Neurosci* **33**:4494–4504.
- 559 Mei N, Grossberg MD, Ng K, Navarro KT, Ellmore TM. 2018. A high-density scalp EEG dataset  
560 acquired during brief naps after a visual working memory task. *Data Brief* **18**:1513–1519.
- 561 Modat M, Ridgway GR, Taylor ZA, Lehmann M, Barnes J, Hawkes DJ, Fox NC, Ourselin S.  
562 2010. Fast free-form deformation using graphics processing units. *Comput Methods  
563 Programs Biomed* **98**:278–284.
- 564 Mukamel R, Fried I. 2012. Human intracranial recordings and cognitive neuroscience. *Annu Rev  
565 Psychol* **63**:511–537.
- 566 Muller L, Brette R, Gutkin B. 2011. Spike-timing dependent plasticity and feed-forward input  
567 oscillations produce precise and invariant spike phase-locking. *Front Comput Neurosci*  
568 **5**:45.
- 569 Muller L, Piantoni G, Koller D, Cash SS, Halgren E, Sejnowski TJ. 2016. Rotating waves during  
570 human sleep spindles organize global patterns of activity that repeat precisely through the  
571 night. *eLife* **5**. doi:10.7554/eLife.17267
- 572 Narizzano M, Arnulfo G, Ricci S, Toselli B, Tisdall M, Canessa A, Fato MM, Cardinale F. 2017.  
573 SEEG assistant: a 3DSlicer extension to support epilepsy surgery. *BMC Bioinformatics*  
574 **18**:124.
- 575 Nelson MJ, Pouget P. 2010. Do electrode properties create a problem in interpreting local field  
576 potential recordings? *J Neurophysiol* **103**:2315–2317.
- 577 Newton Harvey E, Loomis AL, Hobart GA. 1937. Cerebral States during Sleep as Studied by  
578 Human Brain Potentials. *Sci Mon* **45**:191.
- 579 Nir Y, Staba RJ, Andrillon T, Vyazovskiy VV, Cirelli C, Fried I, Tononi G. 2011. Regional slow  
580 waves and spindles in human sleep. *Neuron* **70**:153–169.
- 581 Pan S, Mayoral SR, Choi HS, Chan JR, Kheirbek MA. 2020. Preservation of a remote fear  
582 memory requires new myelin formation. *Nat Neurosci* **23**:487–499.

- 583 Perol T, Gharbi M, Denolle M. 2018. Convolutional neural network for earthquake detection and  
584 location. *Sci Adv* **4**:e1700578.
- 585 Peyrache A, Battaglia FP, Destexhe A. 2011. Inhibition recruitment in prefrontal cortex during  
586 sleep spindles and gating of hippocampal inputs. *Proc Natl Acad Sci U S A* **108**:17207–  
587 17212.
- 588 Piantoni G, Halgren E, Cash SS. 2016. Spatiotemporal characteristics of sleep spindles depend  
589 on cortical location. *Neuroimage* **146**:236–245.
- 590 Rasch B, Born J. 2013. About sleep's role in memory. *Physiol Rev* **93**:681–766.
- 591 Rasch B, Born J. 2007. Maintaining memories by reactivation. *Curr Opin Neurobiol* **17**:698–703.
- 592 Richards MA. 2005. Fundamentals of radar signal processing. Tata McGraw-Hill Education.
- 593 Roy DS, Park Y-G, Ogawa SK, Cho JH, Choi H, Kamensky L, Martin J, Chung K, Tonegawa S.  
594 n.d. Brain-wide mapping of contextual fear memory engram ensembles supports the  
595 dispersed engram complex hypothesis. doi:10.1101/668483
- 596 Sarasso S, Proserpio P, Pigorini A, Moroni F, Ferrara M, De Gennaro L, De Carli F, Lo Russo  
597 G, Massimini M, Nobili L. 2014. Hippocampal sleep spindles preceding neocortical sleep  
598 onset in humans. *Neuroimage* **86**:425–432.
- 599 Schabus M, Dang-Vu TT, Albouy G, Balteau E, Boly M, Carrier J, Darsaud A, Degueldre C,  
600 Desseilles M, Gais S, Phillips C, Rauchs G, Schnakers C, Sterpenich V, Vandewalle G,  
601 Luxen A, Maquet P. 2007. Hemodynamic cerebral correlates of sleep spindles during  
602 human non-rapid eye movement sleep. *Proc Natl Acad Sci U S A* **104**:13164–13169.
- 603 Schabus M, Gruber G, Parapatics S, Sauter C, Klösch G, Anderer P, Klimesch W, Saletu B,  
604 Zeithofer J. 2004. Sleep spindles and their significance for declarative memory  
605 consolidation. *Sleep* **27**:1479–1485.
- 606 Schüz A, Braitenberg V. 2002. The human cortical white matter: quantitative aspects of cortico-  
607 cortical long-range connectivity. *Cortical areas: Unity and diversity* 377–385.
- 608 Sejnowski TJ, Destexhe A. 2000. Why do we sleep? *Brain Res* **886**:208–223.
- 609 Sholl DA. 1956. The organization of the cerebral cortex. John Wiley.
- 610 Silber MH, Ancoli-Israel S, Bonnet MH, Chokroverty S, Grigg-Damberger MM, Hirshkowitz M,  
611 Kaper S, Keenan SA, Kryger MH, Penzel T, Pressman MR, Iber C. 2007. The visual  
612 scoring of sleep in adults. *J Clin Sleep Med* **3**:121–131.
- 613 Song S, Miller KD, Abbott LF. 2000. Competitive Hebbian learning through spike-timing-  
614 dependent synaptic plasticity. *Nat Neurosci* **3**:919–926.
- 615 Steriade M. 2003. The corticothalamic system in sleep. *Front Biosci* **8**:d878–99.
- 616 Takeuchi S, Murai R, Shimazu H, Isomura Y, Mima T, Tsujimoto T. 2016. Spatiotemporal  
617 Organization and Cross-Frequency Coupling of Sleep Spindles in Primate Cerebral Cortex.  
618 *Sleep* **39**:1719–1735.
- 619 Tulving E. 1983. Elements of Episodic Memory. Oxford University Press.
- 620 Wang F, Ren S-Y, Chen J-F, Liu K, Li R-X, Li Z-F, Hu B, Niu J-Q, Xiao L, Chan JR, Mei F. 2020.  
621 Myelin degeneration and diminished myelin renewal contribute to age-related deficits in  
622 memory. *Nat Neurosci* **23**:481–486.
- 623 Warby SC, Wendt SL, Welinder P, Munk EGS, Carrillo O, Sorensen HBD, Jennum P, Peppard  
624 PE, Perona P, Mignot E. 2014. Sleep-spindle detection: crowdsourcing and evaluating  
625 performance of experts, non-experts and automated methods. *Nat Methods* **11**:385.
- 626 Wheeler ME, Petersen SE, Buckner RL. 2000. Memory's echo: Vivid recollection activates  
627 modality specific cortex. *Proceedings of the National Academy of Sciences* **97**:11125–  
628 11129.
- 629 Yanagawa T, Chao ZC, Hasegawa N, Fujii N. 2013. Large-Scale Information Flow in Conscious  
630 and Unconscious States: an ECoG Study in Monkeys. *PLoS ONE*.  
631 doi:10.1371/journal.pone.0080845